Elastic shape analysis computations for clustering left atrial appendage geometries of atrial fibrillation patients

Zan Ahmad[1,2], Minglang Yin[2], Yashil Sukurdeep[1], Noam Rotenberg[2], Eugene Kholmovski[2], and Natalia A. Trayanova[1,2]

[1] Department of Applied Mathematics and Statistics, Johns Hopkins University, Baltimore MD 21210, USA
[2] Department of Biomedical Engineering, Alliance for Cardiovascular Diagnostics and Treatment Innovation (ADVANCE), Baltimore, MD, 21210, USA

Abstract. Morphological variations in the left atrial appendage (LAA) are associated with different levels of ischemic stroke risk for patients with atrial fibrillation (AF). Studying LAA morphology can elucidate mechanisms behind this association and lead to the development of advanced stroke risk stratification tools. However, current categorical descriptions of LAA morphologies are qualitative and inconsistent across studies, which impedes advancements in our understanding of stroke pathogenesis in AF. To mitigate these issues, we introduce a quantitative pipeline that combines elastic shape analysis with unsupervised learning for the categorization of LAA morphology in AF patients. As part of our pipeline, we compute pairwise *elastic distances* between LAA meshes from a cohort of 20 AF patients, and leverage these distances to cluster our shape data. We demonstrate that our method clusters LAA morphologies based on distinctive shape features, overcoming the innate inconsistencies of current LAA categorization systems, and paving the way for improved stroke risk metrics using objective LAA shape groups.

Keywords: elastic shape analysis · computational anatomy · left atrial appendage · ischemic stroke · atrial fibrillation.

1 Introduction

Atrial fibrillation (AF) is the most common cardiac arrhythmia, characterized by irregular contractions of the atrial chambers [1]. It represents an emerging global health crisis, affecting $2-3\%$ of individuals worldwide, with its prevalence expected to increase 2.5-fold in the next 40 years [2]. This rhythm disorder is associated with blood stagnation and clot formation in the left atrial appendage (LAA) – a tubular pouch attached to the main body of the left atrium [3]. A devastating complication of AF occurs when clots detach from the LAA and travel to the brain, causing vessel blockage and leading to ischemic stroke [4]. The risk of stroke in AF patients is five times that of a healthy individual [5].

Numerous studies have shown that LAA morphology is correlated with different levels of ischemic stroke risk [6,7,8,9]. Despite this evidence, the ubiquitously employed stroke risk stratification metrics for AF patients overlook geometric considerations of the LAA [10]. Furthermore, these metrics often inaccurately determine which patients should receive oral anticoagulants, which can cause severe side effects such as internal bleeding and intracranial hemorrhage [10,11,12,13,14,15,16]. Additionally, in current LAA shape classification systems, the "chicken-wing" appendage is known to exhibit lower stroke prevalence compared to other categories (e.g., windsock, cauliflower, cactus) [9,17]. However, the high inter-observer variability in these qualitative classification systems has led to inconsistent definitions of LAA morphology categories across different studies and patient populations [18]. Consequently, mixed conclusions have been documented regarding the association between LAA morphologies and ischemic stroke risk, hindering the incorporation of LAA shape information into stroke risk assessments [19]. Therefore, an objective framework for LAA shape categorization is imperative.

Some studies quantify LAA shape using simple metrics and functional data [20,21,7], but only a few studies have used detailed shape analysis approaches. Slipsager et al. developed a framework for the statistical shape analysis and clustering of LAA geometries based on non-rigid volumetric registration of signed distance fields, and Juhl et al. further extended this work [22,23]. These methods face limitations as they require point-to-point correspondences between LAA meshes (i.e., parametrized 3D surfaces) for statistical shape analysis.

In this paper, we propose a novel computational pipeline for LAA morphology categorization which combines automated atrial segmentation, mesh generation, *elastic distance* computations, and hierarchical clustering. For 3D LAA meshes from 20 AF patients, we compute and leverage pairwise elastic distances to (a): quantify the similarity between pairs of shapes by calculating the Riemannian energy required to deform one of them into the other, and (b): cluster the meshes into distinct categories based on these shape similarities. Our pipeline has the ability to operate on unparametrized surfaces, which circumvents the requirement of point-to-point correspondences between LAA geometries, and renders the pipeline readily implementable in clinical workflows.

2 Methods

In what follows, we describe our LAA data, provide theoretical background on elastic shape analysis (ESA), and detail our computational approach for clustering the LAA geometries.

2.1 Data Description and Preparation

A dataset of 20 de-identified contrast-enhanced computed tomography (CT) scans of AF patients was used in this study. We adapted a deep learning model to automate LA segmentations on the CT scans [24]. The model has a cascade

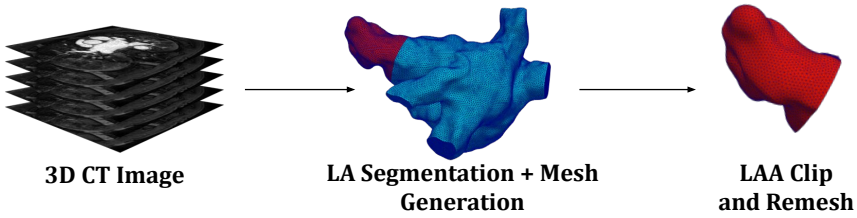

Fig. 1. Schematic summary of the pre-processing pipeline: From 3D CT images, we automatically segment the LA using a deep learning approach, and generate a triangulated 3D mesh. Then the LAA (red) is clipped from the LA body (blue) and re-meshed.

structure, where a region of interest is first cropped and followed by a convolutional neural network (CNN) that performs segmentation on the cropped area. All CNN-segmented scans were examined manually by an imaging expert ***** for quality check. From the LA segmentations, we isolated the LAA from the LA chamber using `Paraview`'s clip tool, such that the ostium was orthogonal to the initial protrusion of the appendage from the main body of the chamber, based on the LAA segmentation approach in [25]. We then re-meshed the clipped LAA to yield the fully pre-processed geometry for shape analysis, see Figure 1.

2.2 Elastic Shape Analysis

The "shapes" of interest to us in this article are LAA meshes, which we model mathematically (from a continuous viewpoint) as surfaces immersed in $\mathbb{R}^3$. As such, our approach for LAA shape comparison and categorization relies fundamentally on a quantitative measure of similarity (i.e., a distance) between surfaces. The framework of Riemannian shape analysis is particularly well-suited for defining such notions, whereby at a high level, distances between pairs of geometric objects (such as LAA meshes) correspond to the minimal amount of 'energy' required to morph one of the objects into the other via a combination of geometric transformations such as bending and stretching [26,27,28,29]. In what follows, we outline the theoretical underpinnings of this framework.

Let us start by defining a *parametrized immersed surface* in $\mathbb{R}^3$, which refers to a smooth mapping $q \in C^\infty(M, \mathbb{R}^3)$, whose differential dq is injective at every point of the parameter space M, which is a 2-dimensional compact manifold (possibly with boundary) whose local coordinates are denoted by $(u, v) \in \mathbb{R}^2$. For example, M can be a compact domain of $\mathbb{R}^2$ if one is working with open LAA meshes, or the sphere $\mathbb{S}^2$ in the setting of closed LAA meshes. The set of all parametrized surfaces, denoted by $\mathcal{I}$, is itself an infinite-dimensional manifold, where the tangent space at any $q \in \mathcal{I}$, denoted $T_q\mathcal{I}$, is given by $C^\infty(M, \mathbb{R}^3)$. Any tangent vector $h \in T_q\mathcal{I}$ can be thought of as a vector field along the surface q.

The key ingredient in Riemannian shape analysis is to equip the manifold $\mathcal{I}$ with a Riemannian metric G, which in our case refers to a family of inner products $G_q : T_q\mathcal{I} \times T_q\mathcal{I} \to \mathbb{R}$ that varies smoothly with respect to $q \in \mathcal{I}$.

Indeed, any Riemannian metric G on $\mathcal{I}$ induces a (pseudo) distance on this space, which is given for any two parametrized surfaces $q_0, q_1 \in \mathcal{I}$ by

$$d_G(q_0, q_1)^2 = \inf_{q(\cdot) \in \mathcal{P}_{q_0}^{q_1}} \int_0^1 G_{q(t)}(\partial_t q(t), \partial_t q(t))\ dt, \tag{1}$$

where the infimum is taken over the space of all paths of immersed surfaces connecting q_0 and q_1, which we write as

$$\mathcal{P}_{q_0}^{q_1} := \{q(\cdot) \in C^\infty([0,1], \mathcal{I}) : q(0) = q_0, q(1) = q_1\}, \tag{2}$$

with $\partial_t q(t)$ denoting the derivative of this path with respect to time t. We refer to the minimization problem in (1) as the *parametrized matching problem*, where q_0 and q_1 are called the *source* and *target* surfaces respectively, with d_G being known as the *geodesic distance* between q_0 and q_1, and where minimizing paths $q(\cdot) \in \mathcal{P}_{q_0}^{q_1}$ (if they exist) are termed *geodesics*. The functional being minimized in (1) is called the *Riemannian energy* of the path $q(\cdot)$, and thus, geodesics can be interpreted as optimal deformations of minimal 'energy' between q_0 and q_1. In a Riemannian setting, geodesics and distances obtained via (1) form the basis of frameworks for the comparison and statistical shape analysis of surfaces, see [28].

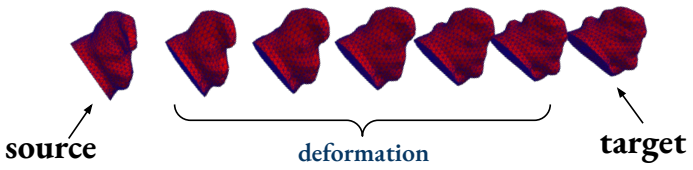

Fig. 2. Example computation of the geodesic (optimal deformation) between a source LAA surface (q_0) and target LAA surface (q_1) to obtain the geodesic distance $d_G(q_0, q_1)$.

Nevertheless, we need to look beyond the setting of parametrized surfaces, i.e., geometric data with known point-to-point correspondences. Indeed, our goal is to develop a method for the comparison of LAA morphologies on datasets of unregistered LAA meshes, independently of how they are parametrized (or sampled/discretized). To this end, we introduce the *reparametrization group* $\mathcal{D}$, i.e., the group of all diffeomorphisms (smooth and bijective maps $\varphi \in C^\infty$) of the parameter space M. For any surface $q \in \mathcal{I}$ and $\varphi \in \mathcal{D}$, we say that $q \circ \varphi \in \mathcal{I}$ is a *reparametrization* of q by φ. The discrete analogue of a reparametrization of a surface is a re-meshing of a discretized (e.g. triangulated) 3D mesh.

Since we seek geodesic distances between shapes regardless of how they are parametrized, let us introduce the *shape space of unparametrized surfaces*, defined as the quotient space of parametrized surfaces modulo the reparametrization group $\mathcal{S} = \mathcal{I}/\mathcal{D}$, which consists of equivalence classes $[q] = \{q \circ \varphi | \varphi \in \mathcal{D}\}$ comprised of all reparametrizations of a given surface $q \in \mathcal{I}$. To obtain a distance

on the shape space, we require a Riemannian metric G that is invariant under the action of the aforementioned reparametrization group $\mathcal{D}$, i.e., we require

$$G_q(h,k) = G_{q\circ\varphi}(h\circ\varphi, k\circ\varphi) \tag{3}$$

for all $q \in \mathcal{I}$, $h,k \in T_q\mathcal{I}$ and $\varphi \in \mathcal{D}$. The field of *elastic shape analysis* (ESA) is a particularly powerful source of Riemannian metrics satisfying the reparametrization-invariance property above [26,27].

In this paper, we shall focus on *second-order Riemannian Sobolev metrics (H^2-metrics)*, which have been shown to possess several desirable properties including the reparametrization-invariance property in (3), and which have successfully been used in applications with unregistered 3D geometric data [26,28,30,31]. For all $q \in \mathcal{I}$ and $h,k \in T_q\mathcal{I}$, the family of H^2-metrics is defined as:

$$\begin{aligned} G_q(h,k) = \int_M \Big(& a_0\langle h,k\rangle + a_1 g_q^{-1}(dh_m, dk_m) \\ & + b_1 g_q^{-1}(dh_+, dk_+) + c_1 g_q^{-1}(dh_\perp, dk_\perp) \\ & + d_1 g_q^{-1}(dh_0, dk_0) + a_2\langle \Delta_q h, \Delta_q k\rangle \Big)\, \mathrm{vol}_q, \end{aligned} \tag{4}$$

where $a_0, a_1, b_1, c_1, d_1, a_2$ are non-negative weighting coefficients for the different zeroth, first and second order terms in the metric. In the above, dh is the vector valued one-form on M given by the differential of h, i.e., a map from TM to $\mathbb{R}^3$ which can be viewed as a 3×2 matrix field on M (in a given coordinate system). Meanwhile, $g_q = q^*\langle\cdot,\cdot\rangle$ is the pullback of the Euclidean metric on $\mathbb{R}^3$, which can be represented as a 2×2 symmetric positive definite matrix field on M, implying that $g_q^{-1}(dh,dh) = \mathrm{tr}(dh\ g_q^{-1}\ dh^T)$. Finally, the second-order term involves the Laplacian Δ_q induced by q, which can be written in coordinate-form as $\Delta_q h = \frac{1}{\sqrt{\det(g_q)}}\partial_u\left(\sqrt{\det(g_q)}\ g_q^{uv}\partial_v h\right)$. We note that the first-order term in the metric is split as a result of the orthogonal decomposition of dh into the sum of $dh_m, dh_+, dh_\perp$ and dh_0, where the precise definitions of these terms are given in [28]. The important thing to note about splitting the metric in this way is that the terms weighted by a_1, b_1, c_1 in (4) correspond to shearing, stretching and bending energies induced by the deformation field h respectively. Therefore, the class of invariant H^2-metrics provides us with the flexibility to emphasize or penalize different types of deformations when computing geodesics via the selection of the weighting coefficients. This is particularly useful when working LAA meshes, as it allows us to incorporate prior knowledge about LAA geometry when selecting parameters to compute pairwise distances, which helps us obtain meaningful distances for downstream tasks such as clustering.

With a reparametrization-invariant Riemannian metric G in hand, such as an H^2-metric from (4), its associated geodesic distance function d_G given in (1) descends to a distance $d_{\mathcal{S}}$ on the quotient shape space $\mathcal{S}$, which is given for any

$[q_0], [q_1] \in \mathcal{S}$ by:

$$d_{\mathcal{S}}([q_0],[q_1])^2 = \inf_{\varphi \in \mathcal{D}} d_G(q_0, q_1 \circ \varphi)^2 = \inf_{\varphi \in \mathcal{D}} \inf_{q(\cdot) \in \mathcal{P}_{q_0}^{q_1 \circ \varphi}} \int_0^1 G_{q(t)}(\partial_t q(t), \partial_t q(t)) dt. \tag{5}$$

To compute geodesic distances on the shape space, we thus need to solve the *unparametrized matching problem* above, which involves finding an optimal path of immersions from q_0 (having a fixed parametrization) to an optimal reparametrization of q_1, i.e., we require an optimal path such that $q(0) = q_0$ and $q(1) = q_1 \circ \varphi$.

In practice, solving (5) numerically is challenging. Indeed, it is relatively straightforward to discretize the H^2-metric and Riemannian energy functional by considering surfaces discretized as triangulated meshes [28], which allows us to frame the minimization over paths of surfaces as a standard finite-dimensional optimization problem. Yet, the optimizitation over reparametrizations of q_1 is challenging as the discretization of the diffeomorphism group $\mathcal{D}$ and its action on surfaces is not straightforward, see [27,32]. This motivates the need for alternative techniques for solving (5). One approach, recently proposed in [28,33], deals indirectly with the minimization over reparametrizations of q_1 by instead introducing a relaxation of the end time constraint $q(1) \approx q_1 \circ \varphi$ using a *data attachment term* $\mathit{\Gamma}([q(1)],[q_1])$ that is independent of the parametrizations of either $q(1)$ or q_1. Broadly speaking, this approach involves solving the *relaxed matching problem* below:

$$\inf \left\{ \int_0^1 G_{q(t)}(\partial_t q(t), \partial_t q(t)) dt + \lambda \mathit{\Gamma}([q(1)],[q_1]) \right\}, \tag{6}$$

where the minimization occurs over paths of surfaces $q(\cdot) \in C^\infty([0,1], \mathcal{I})$ that satisfy the initial constraint $q(0) = q_0$ *only*, and where $\mathit{\Gamma}([q(1)],[q_1])$ is a term that measures the discrepancy between the endpoint of the path $q(1)$ and the true target surface q_1, with $\lambda > 0$ being a balancing parameter. In particular, this approach allows us to bypass the optimization over the diffeomorphism group $\mathcal{D}$. In this paper, we follow the approach of past works with unregistered surface data [33,28,30] and define $\mathit{\Gamma}$ specifically as a kernel metric on the space of varifolds. While we omit the technical details behind the construction of these so-called varifold fidelity metrics in this paper for concision, we refer interested readers to the works of [34,35] for further details.

To bring everything together, our approach for computing pairwise distances for the comparison and categorization of LAA morphologies involves discretizing the LAA geometries as triangulated 3D meshes, and solving the relaxed matching problem (6) numerically using the approach of [28], where the Riemannian metric G is an H^2-metric (4), and where the data attachment term $\mathit{\Gamma}$ is the varifold fidelity metric defined in [28]. For clarity, in the results for LAA shape categorization presented in Section 3, and in particular in Figure 3a, the distances we report are estimates $\tilde{d}_{\mathcal{S}}(q_0, q_1)$ for the true shape distance $d_{\mathcal{S}}(q_0, q_1)$ between a given a pair of LAA meshes q_0 and q_1, which are given by $\tilde{d}_{\mathcal{S}}(q_0, q_1) \doteq \int_0^1 G_{q(t)}(\partial_t q(t), \partial_t q(t)) dt$, where the expression on the right is evaluated at an optimal path of surfaces $q(\cdot)$ found by solving (6).

2.3 Hierarchical Clustering of LAA Geometries

Equipped with elastic distances, we use hierarchical clustering (with Ward's linkage method) to cluster the LAA geometries. Hierarchical clustering is a method used to group a set of objects into categories (clusters) based on their similarity to each other, which is quantified using a distance metric. This approach is particularly useful for categorizing 3D shapes based on pairwise distances within a high-dimensional manifold [36].

Specifically, given a set of shapes $\{q_1, \ldots, q_n\} \in \mathcal{S}$, where $D \in \mathbb{R}^{n \times n}$ is the symmetric matrix whose entries D_{ij} represent the distance between shape q_i and q_j (e.g., elastic distances $d_{\mathcal{S}}(q_i, q_j)$ computed via (6)), hierarchical clustering operates as follows: Initially, each shape is considered a separate cluster, leading to n clusters, $C \doteq \{c_1, \ldots, c_n\}$ where $c_i = \{q_i\}$. We iteratively merge the closest clusters by identifying c_a and c_b that minimize the increase in total within-cluster variance, defined below:

$$\Delta\mathrm{Var}(c_a, c_b) = \mathrm{Var}(c_{new}) - \mathrm{Var}(c_a) - \mathrm{Var}(c_b), \tag{7}$$

where $\mathrm{Var}(c)$ is defined as the average of the squared distances between each point in a given cluster c and the cluster's centroid. At each iteration, the two closest clusters c_a and c_b are merged into a new cluster $c_{new} = c_a \cup c_b$, and $C \leftarrow (C \setminus \{c_a, c_b\}) \cup \{c_{new}\}$ is updated accordingly. This process iterates until all shapes are grouped into a desired number of clusters.

2.4 Multidimensional Scaling to Visualize Clusters

After clustering, we employ multi-dimensional scaling (MDS) to visualize LAA shape clusters in a lower-dimensional Euclidean space [37]. That is, given a set of LAA shapes $\{q_1, \ldots, q_n\} \in \mathcal{S}$ with corresponding geodesic distance function $d_{\mathcal{S}}$, we use MDS to find $\hat{x}_1, \ldots, \hat{x}_n \in \mathbb{R}^m$ (for some $m \in \mathbb{N}$) such that

$$\hat{x}_1, \ldots, \hat{x}_n = \underset{y_1, \ldots, y_n \in \mathbb{R}^m}{\operatorname{argmin}} \Big(\sum_{i \neq j} (d_{\mathcal{S}}(q_i, q_j) - \|y_i - y_j\|)^2 \Big)^{\frac{1}{2}}, \tag{8}$$

which yields a mapping of the LAA geometries as points in $\mathbb{R}^m$, while preserving relative information about their pairwise distances in the original shape space.

3 Results

Figure 3 presents results of our quantitative pipeline for LAA morphology categorization on the cohort of LAA geometries.

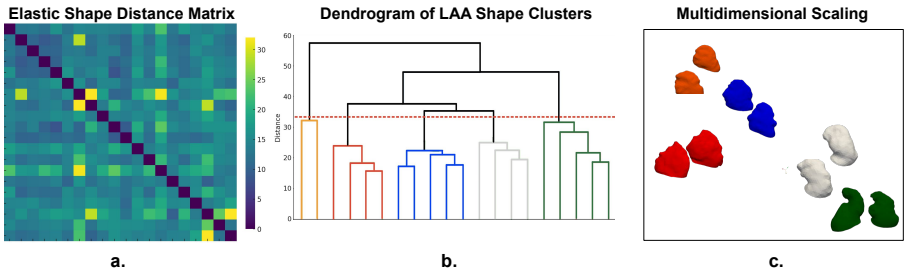

Fig. 3. (a) Symmetric matrix representing pairwise elastic distances computed for our cohort of 20 LAA geometries described in Section 2.1. (b) Dendrogram illustrating LAA shape clusters obtained via hierarchical clustering, with the threshold (red dashed line) used to separate the geometries into five clusters. (c) MDS plot of the LAA geometries with 10 LAA shapes plotted over their embeddings in 2D Euclidean space. Two LAA meshes from each category are shown and color-matched to clusters in the dendrogram.

The computed elastic distances between all pairs of LAA meshes in the cohort are displayed in the distance matrix in Figure 3a. Each element of the matrix takes approximately 1-3 minutes to compute on a GPU. These distance estimates, obtained via the relaxed matching problem (6), are not a priori symmetric due to the varifold relaxation term. We therefore selected a subset of our LAA meshes and computed $d_{\mathcal{S}}(q_i, q_j)$ and $d_{\mathcal{S}}(q_j, q_i)$ for all pairs of meshes q_i, q_j in this subset. We found the computed distances to be within a round off error of each other (i.e., $d_{\mathcal{S}}(q_i, q_j) \approx d_{\mathcal{S}}(q_j, q_i)$), and therefore only computed the upper-triangular part of the matrix in Figure 3, before symmetrizing it.

After computing the pairwise distances, we applied hierarchical clustering and MDS to categorize and visualize the LAA clusters based on their geometric similarities, with results shown in Figures 3b and 3c. The dendrogram illustrating the hierarchical clustering results in Figure 3b facilitated the selection of a threshold (the red dashed line) for the identification of five distinct LAA shape clusters. We projected these LAA shape clusters into 2D Euclidean space via MDS in Figure 3c, where we have plotted a subset of 10 representative geometries (two from each cluster) to avoid overcrowding the figure.

The results demonstrate that, even on a modest dataset of 20 LAA geometries, our pipeline can cluster LAA shapes with similar morphology into the same group while separating different shape types into distinct clusters. Notably, the green and white LAA groups could both be identified as "chicken wing" appendages in current qualitative categorization systems. Yet, our method groups them in different clusters, demonstrating that our pipeline can detect subtle shape features not captured by qualitative classifications, thereby enabling the identification of intermediate shape groups between the qualitative categories.

4 Discussion

Advantages of our approach: Unlike previous studies that necessitate precise point-to-point correspondences for comparing and categorizing LAA shapes, our approach is adapted for unparametrized surfaces, leveraging the relaxed matching approach detailed in (6). Indeed, establishing point correspondences often incurs high computational costs and can yield unsatisfactory results with complex geometric data [22,23]. For instance, Juhl et al. mention that they chose to refine the point correspondence on decoupled LAAs due to the large differences in size and complexity between the LAA and the remaining LA, making it difficult to maintain good correspondences over the entire mesh [23]. Even state-of-the-art methods for finding point correspondences with 3D geometric data, such as the functional maps framework, struggle with fine-grained and intricate geometries, unless a good prior selection of landmarks is provided [38]. By alleviating the need for point correspondences, our approach thus overcomes the computational hurdles often encountered during the registration of complex geometric data such as LAA meshes [22,23,38].

Limitations: Some limitations of our work include the computational time required for pairwise distance calculations on large datasets and the complex parameter tuning process for computing elastic distances which could be improved via the supervised learning approach of [39] to predict the elastic distances, and the parameter selection criteria of [40], respectively. We note, however, that these tasks need only be performed once to solidify shape categories.

Clinical Significance: Our framework's compatibility with unparametrized surfaces enables us to work with LAA meshes with diverse vertex counts and discretization schemes with minimal pre-processing, thereby significantly enhancing its flexibility with data that has been acquired or segmented via different techniques and/or with data from different hospitals. This can enable efficient comparison of new LAA shapes to representative or averaged template shapes from *established* clusters. Avenues for future work include establishing clusters on a larger LAA dataset with stroke history information to refine the shape categorization system and identify clusters with higher stroke prevalence. This effort would allow clinicians to objectively compare new LAA geometries—sourced by various imaging acquisition modalities and healthcare centers— into one of the predefined groups or measure their distance from high-risk groups. This could lead to new metrics for stroke likelihood in AF patients and improve clinical decision-making regarding the administration of preventative medications (such as anticoagulants) with severe side effects [11].

Conclusion: Our integrated approach of performing hierarchical clustering followed by MDS on the elastic distances provides a comprehensive framework for categorizing and visualizing the complex geometric variations of LAA shapes, with applications towards improved stroke risk management in AF patients.

Data Availability: All de-identified data, `Python` code and specific dependencies / packages are available upon request for reproducibility.

Acknowledgements: Z.A. was supported by grant n. 24PRE1196125 - American Heart Association (AHA) predoctoral fellowship and grant n. T32 HL007024 from the National Heart, Lung, and Blood Institute. M.Y. would like to acknowledge support from Heart Rhythm Society Fellowship. N.A.T. acknowledges National Institutes of Health (NIH) grants n. R01HL166759 and R01HL142496 and the Leducq Foundation.

Author Contributions: Z.A., M.Y., Y.S.: Conceptualization, methodology, software implementation, data preprocessing, simulation, formal analysis, writing (original draft). N.R.: Data preprocessing, formal analysis. E.K.: Data acquisition and processing, supervision, formal analysis, writing (review). N.T.: Funding acquisition, conceptualization, supervision, project administration, formal analysis, writing (review).

References

1. Craig T January, L Samuel Wann, Hugh Calkins, Lin Y Chen, Joaquin E Cigarroa, Joseph C Cleveland Jr, Patrick T Ellinor, Michael D Ezekowitz, Michael E Field, Karen L Furie, et al. 2019 aha/acc/hrs focused update of the 2014 aha/acc/hrs guideline for the management of patients with atrial fibrillation: a report of the american college of cardiology/american heart association task force on clinical practice guidelines and the heart rhythm society in collaboration with the society of thoracic surgeons. *Circulation*, 140(2):e125–e151, 2019.
2. Francesca Pistoia, Simona Sacco, Cindy Tiseo, Diana Degan, Raffaele Ornello, and Antonio Carolei. The epidemiology of atrial fibrillation and stroke. *Cardiology clinics*, 34(2):255–268, 2016.
3. Qian Yang, Shuang Liu, Jiang Wang, and Yulong Guo. An observational study: Clinical manifestations and prognosis of left atrial thrombosis in atrial fibrillation. *SN Comprehensive Clinical Medicine*, 5(1):159, 2023.
4. Philip A Wolf, Robert D Abbott, and William B Kannel. Atrial fibrillation as an independent risk factor for stroke: the framingham study. *stroke*, 22(8):983–988, 1991.
5. Jonathan P Piccini and Gregg C Fonarow. Preventing stroke in patients with atrial fibrillation—a steep climb away from achieving peak performance. *JAMA cardiology*, 1(1):63–64, 2016.
6. Xin Tian, Xue-Jing Zhang, Ying-Fang Yuan, Cai-Ying Li, Li-Xia Zhou, and Bu-Lang Gao. Morphological and functional parameters of left atrial appendage play a greater role in atrial fibrillation relapse after radiofrequency ablation. *Scientific Reports*, 10(1):8072, 2020.
7. Erik T Bieging, Alan Morris, Lowell Chang, Lilas Dagher, Nassir F Marrouche, and Joshua Cates. Statistical shape analysis of the left atrial appendage predicts stroke in atrial fibrillation. *The international journal of cardiovascular imaging*, 37(8):2521–2527, 2021.

8. Lance D Burrell, Benjamin D Horne, Jeffrey L Anderson, J Brent Muhlestein, and Brian K Whisenant. Usefulness of left atrial appendage volume as a predictor of embolic stroke in patients with atrial fibrillation. *The American journal of cardiology*, 112(8):1148–1152, 2013.
9. Luigi Di Biase, Pasquale Santangeli, Matteo Anselmino, Prasant Mohanty, Ilaria Salvetti, Sebastiano Gili, Rodney Horton, Javier E Sanchez, Rong Bai, Sanghamitra Mohanty, et al. Does the left atrial appendage morphology correlate with the risk of stroke in patients with atrial fibrillation? results from a multicenter study. *Journal of the American College of Cardiology*, 60(6):531–538, 2012.
10. S Harb, AAH Hussein, WIS Saliba, YU Wu, BX Xu, LC Cho, OMW Wazni, and WAJ Jaber. P5142 effect of anticoagulation on mortality by chadsvasc score in patients with atrial fibrillation: comparison to patients without atrial fibrillation. *European Heart Journal*, 39(suppl_1):ehy566–P5142, 2018.
11. Thorsten Steiner, Jonathan Rosand, and Michael Diringer. Intracerebral hemorrhage associated with oral anticoagulant therapy: current practices and unresolved questions. *Stroke*, 37(1):256–262, 2006.
12. Lin Y Chen, Faye L Norby, Alanna M Chamberlain, Richard F MacLehose, Lindsay GS Bengtson, Pamela L Lutsey, and Alvaro Alonso. Cha2ds2-vasc score and stroke prediction in atrial fibrillation in whites, blacks, and hispanics. *Stroke*, 50(1):28–33, 2019.
13. Juqian Zhang, Radoslaw Lenarczyk, Francisco Marin, Katarzyna Malaczynska-Rajpold, Jedrzej Kosiuk, Wolfram Doehner, Isabelle C Van Gelder, Geraldine Lee, Jeroen M Hendriks, Gregory YH Lip, et al. The interpretation of cha2ds2-vasc score components in clinical practice: a joint survey by the european heart rhythm association (ehra) scientific initiatives committee, the ehra young electrophysiologists, the association of cardiovascular nursing and allied professionals, and the european society of cardiology council on stroke. *EP Europace*, 23(2):314–322, 2021.
14. Katarzyna Dudziñska-Szczerba, Piotr Kułakowski, Ilona Michałowska, and Jakub Baran. Association between left atrial appendage morphology and function and the risk of ischaemic stroke in patients with atrial fibrillation. *Arrhythmia & Electrophysiology Review*, 11, 2022.
15. YiRen Sun, Yunfei Ling, Zijia Chen, Zhengjie Wang, Tao Li, Qi Tong, and Yongjun Qian. Finding low cha2ds2-vasc scores unreliable? why not give morphological and hemodynamic methods a try? *Frontiers in Cardiovascular Medicine*, 9:1032736, 2023.
16. Piotr Lodziński, Monika Gawałko, Monika Budnik, Agata Tymińska, Krzysztof Ozierański, Marcin Grabowski, Agnieszka Janion-Sadowska, Grzegorz Opolski, Radosław Lenarczyk, Zbigniew Kalarus, et al. Trends in antithrombotic management of patients with atrial fibrillation: A report from the polish part of the eurobservational research programme-atrial fibrillation general long-term registry. *Polskie Archiwum Medycyny Wewnetrznej*, 130(3):196–205, 2020.
17. Runxin Fang, Yang Li, Jun Wang, Zidun Wang, John Allen, Chi Keong Ching, Liang Zhong, and Zhiyong Li. Stroke risk evaluation for patients with atrial fibrillation: Insights from left atrial appendage. *Frontiers in Cardiovascular Medicine*, 9:968630, 2022.
18. Jeff M Smit, Judit Simon, Mohammed El Mahdiui, Lili Szaraz, Philippe J van Rosendael, Márton Kolassváry, Balint Szilveszter, Victoria Delgado, Béla Merkely, Pál Maurovich-Horvat, et al. Anatomical characteristics of the left atrium and left atrial appendage in relation to the risk of stroke in patients with versus without

atrial fibrillation. *Circulation: Arrhythmia and Electrophysiology*, 14(8):e009777, 2021.
19. Shadi Yaghi, Andrew D Chang, Ronald Akiki, Scott Collins, Tracy Novack, Morgan Hemendinger, Ashley Schomer, Brain Mac Grory, Shawna Cutting, Tina Burton, et al. The left atrial appendage morphology is associated with embolic stroke subtypes using a simple classification system: a proof of concept study. *Journal of cardiovascular computed tomography*, 14(1):27–33, 2020.
20. Alberto Zingaro, Zan Ahmad, Eugene Kholmovski, Kensue Sakata, Luca Dede', Alan K Morris, Alfio Quarteroni, and Natalia A Trayanova. A comprehensive stroke risk assessment by combining atrial computational fluid dynamics simulations and functional patient data. *bioRxiv*, pages 2024–01, 2024.
21. Katarzyna Słodowska, Elżbieta Szczepanek, Damian Dudkiewicz, Jakub Hołda, Filip Bolechała, Marcin Strona, Maciej Lis, Jakub Batko, Mateusz Koziej, and Mateusz K Hołda. Morphology of the left atrial appendage: introduction of a new simplified shape-based classification system. *Heart, Lung and Circulation*, 30(7):1014–1022, 2021.
22. Jakob M Slipsager, Kristine A Juhl, Per E Sigvardsen, Klaus F Kofoed, Ole De Backer, Andy L Olivares, Oscar Camara, and Rasmus R Paulsen. Statistical shape clustering of left atrial appendages. In *Statistical Atlases and Computational Models of the Heart. Atrial Segmentation and LV Quantification Challenges: 9th International Workshop, STACOM 2018, Held in Conjunction with MICCAI 2018, Granada, Spain, September 16, 2018, Revised Selected Papers 9*, pages 32–39. Springer, 2019.
23. Kristine Aavild Juhl, Jakob Slipsager, Ole de Backer, Klaus Kofoed, Oscar Camara, and Rasmus Paulsen. Signed distance field based segmentation and statistical shape modelling of the left atrial appendage. *arXiv preprint arXiv:2402.07708*, 2024.
24. Arthur L Lefebvre, Carolyna AP Yamamoto, Julie K Shade, Ryan P Bradley, Rebecca A Yu, Rheeda L Ali, Dan M Popescu, Adityo Prakosa, Eugene G Kholmovski, and Natalia A Trayanova. Lassnet: A four steps deep neural network for left atrial segmentation and scar quantification. In *Challenge on Left Atrial and Scar Quantification and Segmentation*, pages 1–15. Springer, 2022.
25. Andrew Schluchter, Chelsea Jan, Katherine Lowe, Davis M Vigneault, Francisco Contijoch, and Elliot R McVeigh. Vascular landmark-based method for highly reproducible measurement of left atrial appendage volume in computed tomography. *Circulation: Cardiovascular Imaging*, 12(12):e009075, 2019.
26. Martin Bauer, Philipp Harms, and Peter W Michor. Sobolev metrics on shape space of surfaces. *arXiv preprint arXiv:1009.3616*, 2010.
27. Ian H Jermyn, Sebastian Kurtek, Hamid Laga, Anuj Srivastava, Gerard Medioni, and Sven Dickinson. *Elastic shape analysis of three-dimensional objects*. Springer, 2017.
28. Emmanuel Hartman, Yashil Sukurdeep, Eric Klassen, Nicolas Charon, and Martin Bauer. Elastic shape analysis of surfaces with second-order sobolev metrics: a comprehensive numerical framework. *International Journal of Computer Vision*, 131(5):1183–1209, 2023.
29. M Faisal Beg, Michael I Miller, Alain Trouvé, and Laurent Younes. Computing large deformation metric mappings via geodesic flows of diffeomorphisms. *International journal of computer vision*, 61:139–157, 2005.
30. Emmanuel Hartman, Emery Pierson, Martin Bauer, Nicolas Charon, and Mohamed Daoudi. Bare-esa: A riemannian framework for unregistered human body

shapes. In *Proceedings of the IEEE/CVF International Conference on Computer Vision*, pages 14181–14191, 2023.
31. Emmanuel Hartman, Emery Pierson, Martin Bauer, Mohamed Daoudi, and Nicolas Charon. Basis restricted elastic shape analysis on the space of unregistered surfaces. *arXiv preprint arXiv:2311.04382*, 2023.
32. Zhe Su, Martin Bauer, Stephen C Preston, Hamid Laga, and Eric Klassen. Shape analysis of surfaces using general elastic metrics. *Journal of Mathematical Imaging and Vision*, 62:1087–1106, 2020.
33. Martin Bauer, Nicolas Charon, Philipp Harms, and Hsi-Wei Hsieh. A numerical framework for elastic surface matching, comparison, and interpolation. *International Journal of Computer Vision*, 129(8):2425–2444, 2021.
34. Irene Kaltenmark, Benjamin Charlier, and Nicolas Charon. A general framework for curve and surface comparison and registration with oriented varifolds. In *Proceedings of the IEEE Conference on Computer Vision and Pattern Recognition*, pages 3346–3355, 2017.
35. Nicolas Charon and Alain Trouvé. The varifold representation of nonoriented shapes for diffeomorphic registration. *SIAM journal on Imaging Sciences*, 6(4):2547–2580, 2013.
36. Fionn Murtagh and Pedro Contreras. Algorithms for hierarchical clustering: an overview. *Wiley Interdisciplinary Reviews: Data Mining and Knowledge Discovery*, 2(1):86–97, 2012.
37. Warren S Torgerson. Multidimensional scaling: I. theory and method. *Psychometrika*, 17(4):401–419, 1952.
38. Maks Ovsjanikov, Mirela Ben-Chen, Justin Solomon, Adrian Butscher, and Leonidas Guibas. Functional maps: a flexible representation of maps between shapes. *ACM Transactions on Graphics (ToG)*, 31(4):1–11, 2012.
39. Emmanuel Hartman, Yashil Sukurdeep, Nicolas Charon, Eric Klassen, and Martin Bauer. Supervised deep learning of elastic srv distances on the shape space of curves. In *Proceedings of the IEEE/CVF conference on computer vision and pattern recognition*, pages 4425–4433, 2021.
40. Martin Bauer, Nicolas Charon, Eric Klassen, Sebastian Kurtek, Tom Needham, and Thomas Pierron. Elastic metrics on spaces of euclidean curves: Theory and algorithms. *arXiv preprint arXiv:2209.09862*, 2022.